Precast CSA-based concrete tunnel lining segments reinforced with GFRP bars: Challenges and opportunities

Simone Spagnuolo [*], Alberto Meda

Department. of Civil Engineering and Computer Science Engineering, University of Rome Tor Vergata, Via del Politecnico 1, Rome 00133, Italy

A R T I C L E   I N F O

A B S T R A C T

This research study investigates the potential of using Calcium Sulfoaluminate (CSA) binder as a sustainable alternative to ordinary Portland cement (OPC) in the production of precast concrete tunnel lining (PCTL) segments. The effectiveness of CSA-based concrete, reinforced with Glass Fiber-Reinforced Polymer (GFRP) bars, was examined through an experimental program. Comparative analyses, including analytical, experimental, and Life Cycle Assessment (LCA) comparisons, were conducted with OPC-based segments reinforced with traditional steel. The results indicate that the proposed CSA/GFRP solution has the potential to improve sustainability in mechanized tunnelling and prefabrication. A case study is also presented to support these findings.

1. Introduction

With an annual worldwide turnover of 125 billion euros and a growth 2.5 times that of the global construction sector, the tunnelling market represents a substantial segment within the civil construction field. Approximately 5200 km of tunnels are constructed each year around the world. As civil engineering is typically 20% of the construction market, tunnelling one represents 7% of the infrastructure sector [1].

Considering both new and existing tunnel projects, periodic maintenance and costly repairs are essential to mitigate the corrosion of steel bars in conventional tunnel linings. Given the significant numbers associated with these structures and the growing emphasis on sustainability for the future, improving the eco-friendly performance of concrete and reinforcement for such structures becomes imperative.

Ordinary Portland cement (OPC) is a crucial component of concrete, and the rising global demand for concrete is driving an increase in OPC production [2,3]. Presently, cement production is responsible for roughly 5–8% of worldwide CO_2 emissions [4,5]. It is therefore imperative to find solutions to reduce CO_2 emissions in the cement sector.

One of the most effective solutions for reducing emissions involves clinker substitution, as defined by the World Business Council for Sustainable Development (WBCSD) and the International Energy Agency (IEA) in the 'Cement Technology Roadmap 2009' [6], as confirmed by [7].

In this context, CO_2 emissions are lower for Calcium Sulfoaluminate (CSA) cement (0.27 tons of CO_2 per ton of CSA cement) compared to Portland cement (0.54 tons of CO_2 per ton of Portland cement), for both materials production and operational processes [8]. The clinkerization process of Portland cement occurs at a temperature of 1450 °C, whereas the operation temperature for CSA cement can be reduced to 1250 °C, resulting in a reduction of 40 kg of CO_2 per ton of CSA cement produced [8]. Moreover, accounting for cement grinding, an additional reduction of 20 kg of CO_2 emissions per ton can be achieved for CSA cement compared to Portland cement [9].

Structurally, the primary benefits of using CSA cement are related to its engineering properties characterized by fast setting, rapid hardening, and high chemical resistance. Due to its ability to develop high early strength with low shrinkage, CSA cement is adopted in the building industry for urgent repairs, soil stabilization, and ceiling applications [10–12]. However, these advantages can turn into disadvantages if pure CSA is used as a binder for the full concrete casting of structural elements, especially when carried out on-site using a concrete mixer truck from the concrete plant.

Interesting performance can be achieved by blending CSA cement with OPC in ternary compositions (Anhydrite-CSA-OPC). This not only enhances the aforementioned advantages but also allows for increased manageable workability, setting time, and high frost resistance [12].

The initial alkalinity of CSA binders (pH ≈ 11–12) is lower than that of OPC binders (pH > 13) but is still capable of passivating steel rebar. Nevertheless, one of the main critical aspects related to the adoption of

CSA-based systems in reinforced concrete structures is represented by the carbonation attack, particularly due to contradictory results found in the literature [13–17].

The primary focus should be on the long-term corrosion risk associated with the penetration of CO2, which can modify the transportation mechanisms of corrosive agents in the carbonated layer and affect compressive strength. It has been demonstrated that ternary systems (Anhydrite-CSA-OPC) are more stable over time in terms of compressive strength and exhibit a lower depth of carbonation than binary systems (Anhydrite-CSA) in which OPC is completely replaced [12]."

In the realm of tunnelling, mechanized excavation stands out as one of the two primary methods for tunnel excavation, widely employed over the past thirty years. Through this method, the tunnel lining is constructed using precast concrete tunnel lining (PCTL) segments, strategically placed by the Tunnel Boring Machine (TBM) and utilized as support elements for its advancement.

The production of PCTL segments, constituting the final lining, typically takes place in precast plants, often situated at a considerable distance from the construction site where they will be installed. The precast plant encompasses production lines and extensive storage areas for segments awaiting the necessary strength before transportation to the construction site.

Two distinct methods can be employed for manufacturing PCTL segments: utilizing static moulds or a carousel system. In the former, segment moulds are stationary within the plant. Following concrete casting, the moulds are covered with thermal blankets (Fig. 1a) to attain sufficient strength for demoulding the segments within the next day.

Conversely, in the carousel production system, moulds traverse various workstations (Fig. 1b) before reaching the fixed casting station. After casting, the mould is then transferred to a steam-curing chamber (Fig. 1c), where curing lasts 6–8 hours.

The steam-curing process still contributes negatively to the environmental impact with an emission of 20 kg of CO2 per cubic meter of manufactured PCTL segment, reduced to 3.7 kg CO2 if the process is optimized by the plant.

Once the PCTL segments are demolded, they are stacked in large areas until the required strength is reached (Fig. 2a). From that point onward, the segments can counteract the TBM thrust during their installation and the excavation progress without suffering structural damage.

Considering these factors, it becomes necessary to account for the number of moulds, curing time, and storage areas, ensuring a sufficient number of stacked segments for 2 or 3 months of excavation and any unforeseen acceleration of the excavation speed. This implies having enough space to stack 6000–9000 segments waiting to be installed. Therefore, to meet these demands, the transport and storage of the segments to the construction site must also be logistically well-organized.

Transporting the segments by trucks from the precast plant to the construction site contributes to increased CO2 emissions and traffic congestion (Fig. 2b). Additionally, having storage spaces on the worksite is not always obvious, depending on the tunnel project and its location. While rural areas pose no issues (Fig. 2c), urban metro tunnels (Fig. 2d) require careful consideration of this aspect.

In light of these challenges, the production of segments, their transport from the precast plant to the construction site, and the need for storage areas in both scenarios are critical aspects with high environmental and socio-economic impacts that must be considered in the design stages.

2. Research significance

Concrete with CSA-based cement has not been utilized for the production of PCTL segments to date. This study was conducted to assess the feasibility of replacing a portion of OPC with CSA binder in the production of PCTL segments, employing a ternary mixture concrete.

To address the lower alkalinity in the concrete mix design and considering long-term carbonation issues, traditional steel reinforcement was substituted with GFRP, which is corrosion-resistant and capable of withstanding low-pH values [18–22]. Moreover, the tensile strength retention of GFRP rebars inside the low-pH CSA concrete is observed to be higher than that inside the OPC concrete [23].

Previous studies have demonstrated the feasibility of using GFRP reinforcement in PCTL segments, proving the effectiveness of GFRP bars as durable reinforcement [24–28]. However, these studies primarily focused on examining the behaviour of precast OPC-based concrete tunnel lining segments. There are no research results available in the literature regarding the behaviour of GFRP-reinforced precast CSA-based concrete segments.

Therefore, the aim of this study is to investigate their behaviour during production, transient phases, and the final stage through experimental full-scale tests. This paper presents the initial results of their kind, making a significant contribution to the relevant literature and providing data to advance the use of CSA-based concrete and GFRP reinforcement in PCTL segments.

The obtained results in this paper are limited to the short-term behaviour of the PCTL segments, and no information is available about their long-term performance. Moreover, the CSA/GFRP proposed solution aligns with global goals to achieve climate neutrality by 2050. In accordance with the stages outlined in the "CO$_2$ Emission in Construction Supply Chain" of Standard UNI EN 15978 [29], the proposed solution aligns with several items in stage A (product and construction stage), such as the use of low carbon concrete, FRP reinforcement, and precast construction. Additionally, for stage B (use and maintenance) of the same Standard, the main solution items include accelerated execution and the use of non-ferrous/FRP rebar. Therefore, the proposed solution enhances the durability of the tunnel, reducing the need for interventions (maintenance, repair, or replacement) during its useful life with a significant reduction in CO$_2$ emissions. The latter, as estimated in the literature, is more than 1.5 times the CO$_2$ emission of the production and construction stage of the structure [30]. This paper illustrates the suitability and sustainability of using CSA-based concrete and GFRP reinforcement in PCTL segments to replace the energy-intensive actual OPC/steel solutions.

In conclusion, this study should serve as a preliminary step towards further research and Life Cycle Assessment (LCA) analysis to evaluate the possibility of developing new prefabrication processes, shifting from the plant to the construction site, ensuring a more sustainable and durable tunnel.
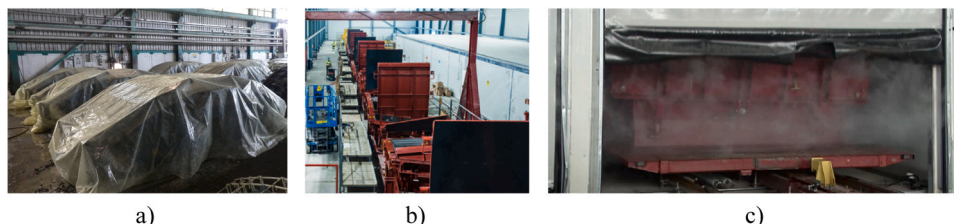

a)	b)	c)

Fig. 1. Segment production methods. a) Static moulds; b) Carousel system; and c) Steam-curing chamber.

Fig. 2. Storage and transport of the precast segments. a) Storage; b) Transport; c) Tunnel construction in rural areas (*image from the website:* www.sabah.com); and d) Tunnel construction in urban areas.

3. Experimental investigation

To demonstrate the effectiveness of the CSA/GFRP proposed solution, segments reinforced with concrete using Ordinary Portland Cement (OPC) and a traditional black steel cage (OPC/Steel) were adopted as a reference. The CSA/GFRP solution was designed with the aim of achieving the same ultimate bending experimental performance as that of the OPC/steel reference.

3.1. Materials

For the concrete mix design, a ternary system was employed to replace pure OPC, based on pozzolanic CEM IV/A (PV) 42.5N SR, typically adopted in Italy for the precast tunnel segments. In the ternary mixture, a fixed ratio between anhydrite (A) and CSA clinker contents (A/CSA) was adopted. A specific amount of limestone Portland cement (CEM II/A-LL 42.5R) was utilized to meet the binder requirements for concrete packaging. The cement mix design comprised 10% A, 35% CSA, and 55% CEM II/A-LL 42.5R.

Calcareous aggregates, utilized in the mix design, included the following particle size fractions: 0–4 mm sand, 8–15 mm gravel, and 15–25 mm rubble. Additionally, a fluidifying additive was introduced to adjust workability and aid in controlling setting times.

Table 1 shows the concrete mix design developed, encompassing density, workability loss, and compressive strength (on three 150 mm side cubic samples for each fixed time reported in Table 1) results obtained from the tests conducted on the concrete, according to UNI EN 12350-6 [48], 12350-2 [49] and 12390-3 [50], respectively. Moreover, standard deviation, in brackets, is also reported.

Based on the results presented in Table 1, the primary advantages are evident in the evolution of compressive strength over time. Indeed, the concrete mix design utilizing CSA cement can achieve the minimum required compressive strength ($f_c = 12 \div 15$ MPa) after just 5 hours, meeting the criteria for demoulding the segments without the need for any steam process. Furthermore, the compressive strength required for

Table 1
Properties of the mix design.

Mix design	Unit	Value
Binder* (A-CSA-CEM II ternary system)	kg/m³	380
Sand	kg/m³	892
Rubble	kg/m³	445
Gravel	kg/m³	503
Additive CC39/P22	%	0.7
Water	l/m³	160
Air content	%	2
Density	kg/m³	2384
Workability loss (Slump)**		
t_0	mm	195
t_{30}	mm	190
t_{60}	mm	180
Compressive strength ($f_{cm,cube}$)		
3 h	MPa	16 (0.64)
5 h	MPa	25 (0.87)
26 h	MPa	40 (1.52)
30 h	MPa	41 (1.55)
7 days	MPa	55 (1.92)
15 days	MPa	57 (1.99)

* Replaces CEM IV/A(P) 42.5N SR pozzolanic cement, normally adopted to cast tunnel segments in Italy;

** t_0 refers to time zero; t_{30} refers to 30 minutes after casting; and t_{60} refers to 60 minutes after casting.

the installation of segments by the TBM erector is reached as early as 26 hours after concrete casting, significantly reducing curing times and the necessity for storage areas for the segments. Concrete shrinkage was measured over time following UNI 11307 standards [31], averaging the values on measurements made on three 200×200×800 mm small beams for each cement type. Fig. 3 displays the results of the concrete shrinkage tests, which were conducted on both the new mix design based on CSA cement and the common mix design typically employed for casting tunnel segments. The latter mix design uses CEM IV/A(PV) 42.5 N SR
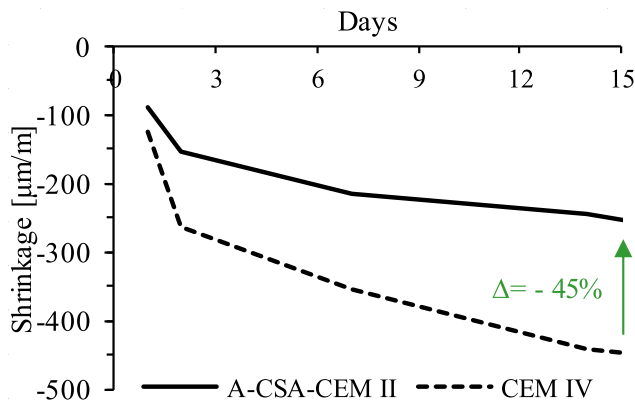
Fig. 3. Shrinkage evolution over time. Solid line refers to common concrete mix design based on pozzolanic cement while dashed line to the new one based on CSA cement.

pozzolanic cement as the binder. It is important to note that both concrete mix designs share the same particle size distribution curve, water content, and binder dosage (380 kg/m3).

Concrete shrinkage measurements commenced 24 hours after the casting for both the proposed CSA-based mix and the reference mix, respectively. According to the results, the concrete mix design using CSA cement exhibits significantly less shrinkage compared to the reference mix based on pozzolanic cement, with a shrinkage of less than 45 percent at 15 days.

The precast segments used in the full-scale test were reinforced with patented closed-loop GFRP bars, obtained through a suitably modified pultrusion process. Each rebar comprises boron-free E-CR fiberglass and a thermoset vinyl ester resin matrix.

The reinforcement included a GFRP cage, where composite bars were designed to optimize the length of each closed-loop ring (Fig. 4). This optimization aimed to fulfill both performance requirements and technical considerations related to mechanical components positioned on the structural elements.

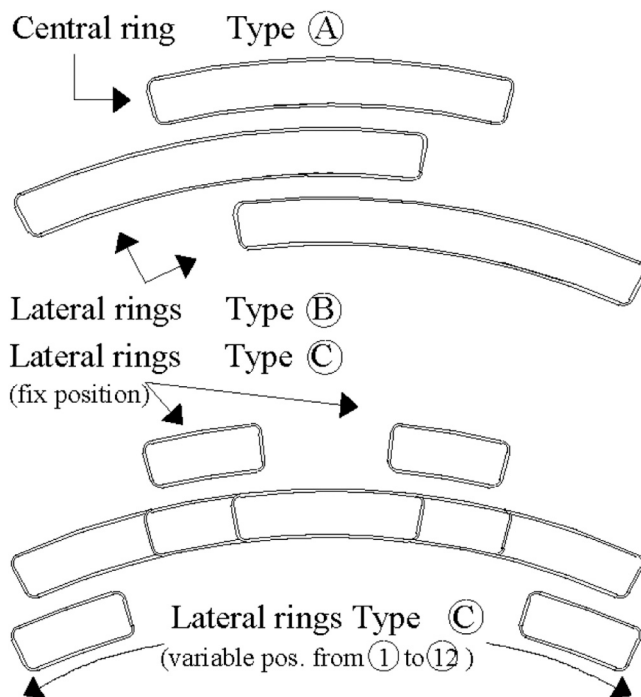Each segment was composed of 12 equivalent Ø13 mm closed-loop

Fig. 4. Longitudinal GFRP reinforcement details.

rings (in the longitudinal direction), each containing superimposed rings (A, B, and C types) of varying lengths, as illustrated in Fig. 4.

The equivalent area of each individual longitudinal GFRP ring was 43.9 mm^2 (comparable to an equivalent bar with a diameter of 7.5 mm), with mean tensile strength and Young's modulus of 1100 MPa and 46 GPa, respectively, obtained according to ASTM 7205 [51] by testing five samples, as detailed in Table 2. Moreover, standard deviation, in brackets, is also reported.

In the transverse direction, the cage was confined by 16 equivalent Ø8 mm GFRP closed-loop stirrups.

In Table 3, the properties of both the OPC/Steel reference and CSA/GFRP proposed segments are summarized. These properties include the type of reinforcements, longitudinal reinforcement ratio, and the strength of both the reinforcement and concrete.

Concerning the segments based on the CSA binder, two segments with different concrete curing times are considered: one at 26 hours (I) and the other at 30 hours and 15 days (II) after casting, respectively. It is important to note that segment (II) was tested under TBM thrust 30 hours after casting and was subsequently subjected to a bending test after aging for 15 days, as will be shown later.

3.2. Full-scale tests

For the full-scale experimental tests, a typical metro tunnel geometry was considered (Fig. 5a). Each precast segment had a thickness of 300 mm, an internal diameter of 5800 mm, and a depth of 1420 mm.

Four precast segments were cast using a truck mixer, employing the same OPC and CSA cement-based concrete mix design for the OPC/Steel reference segments (Fig. 5b) and CSA/GFRP ones (Fig. 5c), respectively.

Full-scale bending tests and point load tests were performed to investigate the flexural capacity of the segments and their behaviour under thrust forces exerted by the TBM during the transient installation phase, respectively. The two full-scale tests, the bending test, and the point load test were carried out at 26 hours and 30 hours of curing for the CSA/GFRP proposed solution and after 28 days of curing for the traditional OPC/Steel reference solution, respectively.

Full-scale bending test was conducted under displacement control, following the testing setup depicted in Fig. 6a. The segment was positioned on two cylindrical supports spaced 3 m apart. Load application was facilitated using an electromechanical jack equipped with a 1000 kN load cell, with a prescribed running speed of 10 μm/sec. The load was uniformly distributed across the mid-span of the segment on the extrados surface through a frame system (Fig. 6a).

Throughout the test, displacements and crack widths on the intrados surface were monitored using three wire transducers and two Linear Variable Differential Transformers (LVDTs), respectively (Fig. 6b). As the load increased, new cracks developed, and their widths were measured using a crack width ruler.

A full-scale point load test, simulating the thrust exerted by a Tunnel

Table 2
Properties of the GFRP bars.

Property	Unit	Value
Longitudinal Ø7.5 GFRP closed-loop ring		
Mean tensile strength$^{(a)}$, f_{fm}	MPa	1100 (40)
Tensile modulus, E_f	GPa	46 (0.90)
Mean tensile strain, ε_{fm}	%	2.39

Note: $^{(a)}$ The tensile strength of the longitudinal closed-loop rings reported in this table, due to the particular configuration of the reinforcement shown in Fig. 5, in which the bent sections of the closed-loop rings are in the area subjected to the main bending actions, will be considered reduced by a partial factor $\gamma_{f,\varnothing}$=2.1. This partial factor is applied to account for the bending effect resulting from a bend radius less than six times ($3d_b$) the equivalent diameter d_b. The value of the partial factor is determined by the ratio of the straight GFRP bar strength to the bent GFRP strength.

Table 3

Tunnel segments properties.

Property →		Segment cross-sectional area		Reinforcement					Concrete			
Solution ↓	Time by the casting	Height [cm]	Width [cm]	Type [-]	Longitudinal [sup+inf]	R[a] [%]	Transversal (stirrups)	f_{ym} [MPa]	$f_{fum}^{[b]}$ [MPa]	Type [-]	$f_{cm,cube}$ [MPa]
OPC/Steel	28 days	30	142	Steel	(12+12) Ø12	0.39	Ø8/20	510	-	Ordinary[d]	48
CSA/GFRP (I)	26 hours	30	142	GFRP	12 rings Ø13eq[c]	0.46	Ø8/20	-	524	Ternary[e]	40
CSA/GFRP (II)	30 h/15d	30	142	GFRP	12 rings Ø13eq[c]	0.46	Ø8/20	-	524	Ternary[e]	41/57

Note:

[a] R= longitudinal reinforcement ratio;

[b] $f_{fum}=f_{fm}/\gamma_{f,\varnothing}=1100/2.1$;

[c] Each segment consisted of 12 equivalent Ø13 mm closed-loop rings (longitudinal direction), each of which in turn, contained superimposed rings (A, B and C types) of different length, according to layout as shown in Fig. 4. The equivalent area of each single longitudinal GFRP ring was equal to 43.9 mm² (comparable to an equivalent bar with diameter equal to 7.5 mm);

[d] Ordinary Portland Cement consists of 100% CEM IV/A(PV) 42.5 N SR pozzolanic cement;

[e] Ternary system consists of 10% anhydrite, 35% CSA, and 55% CEM II/A-LL 42.5 R.
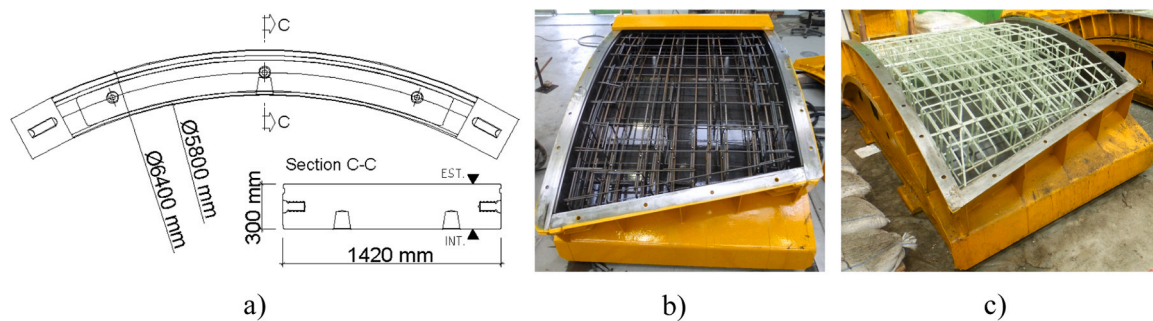

Fig. 5. Full-scale segments: a) Segment's geometry; and b) OPC/Steel segments; c) CSA/GFRP segments.

Boring Machine (TBM) on previously installed segments at the back of the TBM shield during its progress (Fig. 6d), was conducted using the load application setup depicted in Fig. 6c.

The load was applied to each steel pad, in accordance with TBM geometry and configuration, using two 2000 kN hydraulic jacks (4000 kN per steel pad). The testing setup, configured as shown in Fig. 7b, had the capacity to deliver a maximum load of 12000 kN (1200 Tons). The segment was positioned on an appropriately designed reinforced concrete (RC) beam, simulating the segmental tunnel lining behind the ring near the machine.

As illustrated in Fig. 6c, in addition to recording the load, vertical displacements beneath the thrust steel pads and crack widths between them were monitored. Potentiometers (two for each steel pad – intrados/extrados) and two LVDTs were employed for these measurements. Alongside data acquisition, as the load increased incrementally according to TBM specifications (service load), crack patterns were documented. For each significant crack, its width was measured using a crack width ruler.

4. Results and discussion

Based on the obtained results, the ternary system (A-CSA-OPC) can be utilized for concrete production, similar to common Portland cements, offering the advantage of avoiding the need for steam curing of the segment to expedite the demoulding process.

The adopted mix design based on ternary binder exhibit a reduced working time compared to pozzolanic cements commonly used for this application. However, this working time is sufficient for the casting of precast elements. The workability time can be adjusted depending on casting temperatures and requirements through the addition of retardant additives.

A concrete mix based on the A-CSA-OPC ternary system enables achieving a compressive strength exceeding 15 MPa as early as 5 hours after casting, with a workability time of 40 minutes at 30 °C. Time sufficient for concrete casting in prefabrication. Demoulding strengths that are practical for use were already achieved three hours after casting.

Table 4 and Fig. 7 illustrate how cubic strength increases over time, highlighting key points corresponding to the main phases of the experimental program, including demoulding of the segment, bending tests, and TBM tests, respectively.

The development of high early-age strength confirmed the possibility to eliminate the need for the thermal cycle of steam curing, simplifying the precast segment production process both operationally and in terms of plant logistics.

A full-scale bending test was carried out 26 hours after segment casting, achieving an average compressive cubic strength of 40 MPa.

The initial crack appeared at a load level of 139 kN, 140 kN and 130 kN, with a maximum crack width of 0.05 mm, 0.25 mm and 0.05 mm for the OPC/Steel, CSA/GFRP (I) and CSA/GFRP (II) segments, respectively, as depicted in Fig. 8b.

Examining the maximum crack width observed for the CSA/GFRP (I) segment at the cracking load, it is noted that although this value is higher (0.25 mm) compared to that of the reference segment (0.05 mm), it still falls within the ranges specified by Regulations and Codes [34–37]. In fact, Standards specify that the maximum residual crack width for the concrete structures reinforced with GFRP bars should not exceed 0.50 mm.

Regarding the segments reinforced with GFRP bars, the increased concrete strength under flexural loading resulted in narrower cracks and closer crack spacing, as illustrated in Fig. 8b) and Fig. 9b) and c). At the onset of the first crack, a 42% increase in concrete strength corresponded to an 80% reduction in crack width.

With increasing load, multiple cracks emerged of the segments, as depicted in Fig. 9.

The maximum load attained was 373 kN, 380 kN and 395 kN, resulting in a vertical displacement (deflection) of 48 mm, 38 mm and
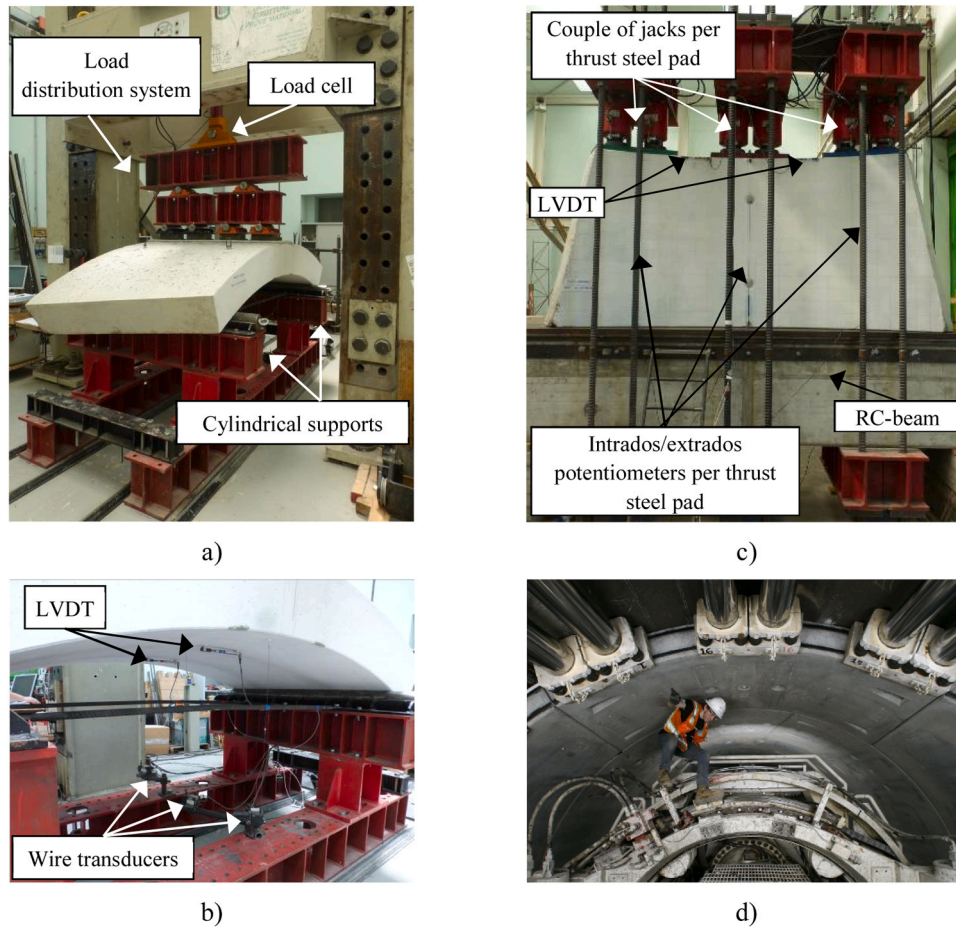
Fig. 6. Full-scale tests: a) Bending test setup; b) Bending test instrumentation at intrados surface; c) TBM thrust test set-up; and d) TBM thrust during its progress.
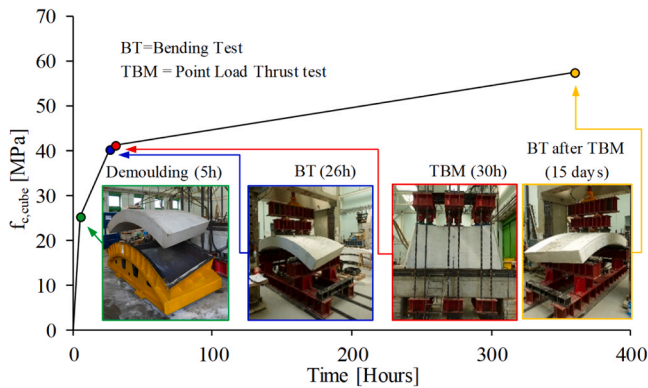

Fig. 7. Development of the strength over time and relevant phases of the experimental campaign for the CSA/GFRP segments.

Table 4
Development of the strength over time and corresponding actions.

Phase	Action	$f_{cm,cube}$ [MPa]	Time [Hours]
t_0	Start of the casting	0	0
t_5: 5 hours after casting	Demoulding	25	5
t_{26}: 26 hours after casting	Bending test	40	26
t_{30}: 30 hours after casting	TBM test	41	30
t_{360}: 15 days after casting	Bending test*	57	360

Note: * the bending test was carried out on the same segment used for the TBM test at t_{30}

31 mm at the mid-span of the segment for the OPC/Steel, CSA/GFRP (I) and CSA/GFRP (II) segments, respectively, as illustrated in Fig. 8a. The collapse of the three segments occurred by tensile failure of the reinforcement at the intrados side. Fig. 10 shows the GFRP bars tensile failure for the CSA/GFRP (I) segment.

Notably, the measurements recorded by the two LVDTs are not considered, as the cracks during the test extended beyond their measurement range.

The capacity of a structural member to endure inelastic deformation without diminishing its load-bearing ability is a fundamental criterion, denoted as structural ductility. In contrast to conventionally steel-reinforced concrete segments for which the ductility can be expressed by the ratio of ultimate to yield deflection points, the GFRP-reinforced segments do not yields. Consequently, the standard definition of the ductility index is not applicable. The ductility of GFRP-reinforced segments can be evaluated based on factors such as energy absorption, as proposed by Naaman and Jeong [32].

The ductility index (μ_e) for the examined segments can be calculated using Eq. 1.

$$\mu_e = 0.5 \bullet (E_{tot}/E_{el} + 1) \tag{1}$$

where E_{tot} represents the total energy calculated as the area under the load–deflection curve up to failure of the segment, and E_{el} denotes the elastic energy (part of the total energy) released at failure. E_{el} can be evaluated as the area of the triangle formed at the failure load of the segment by the line with the weighted average slope of the two initial straight lines of the load–deflection curve, as depicted in Fig. 11.

It is crucial to recognize that substantial deformations preceding failure do not necessarily imply ductility, as demonstrated by the
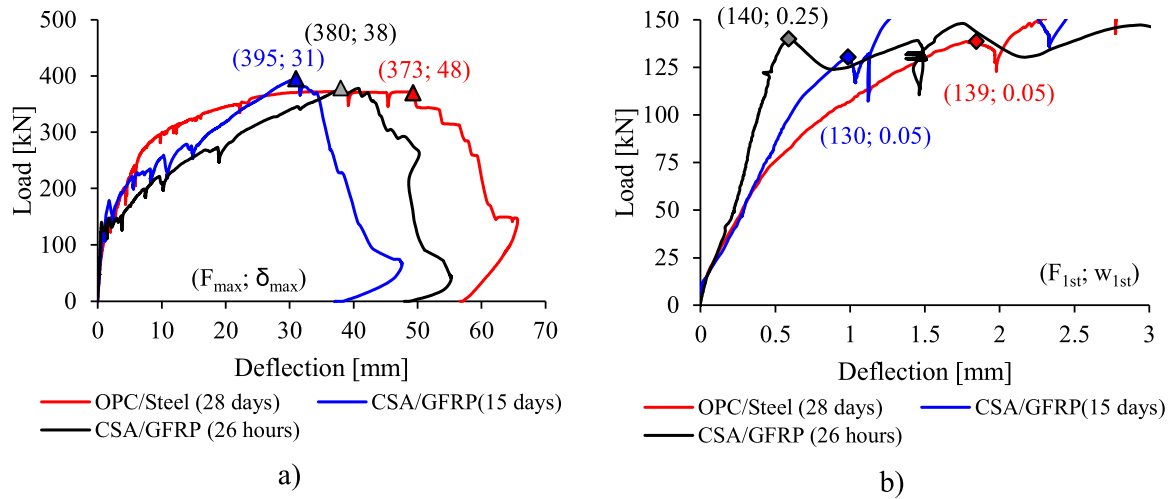
Fig. 8. Bending results: a) Load versus deflection curves; and b) First crack detail of load versus deflection curves;.
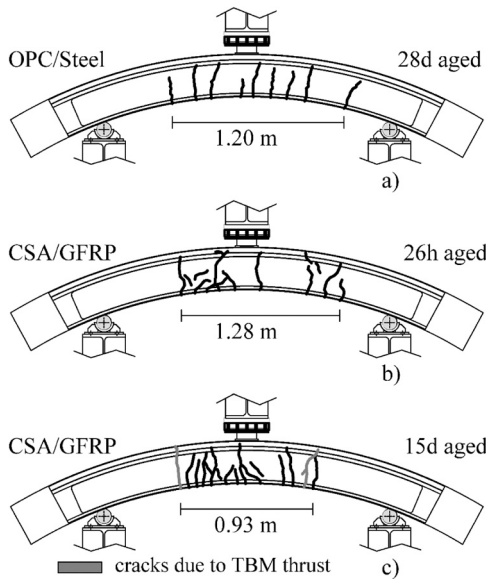

Fig. 9. Cracking patter at failure in: a) OPC/Steel reference segment (28 days aged); b) CSA/GFRP (I) segment (26 hours aged); and c) CSA/GFRP (II) segment (15 days aged – tested after TBM thrust).

Fig. 10. Bending test results of CSA/GFRP (I) segment (26 hours aged): detail of the tensile failure of the GFRP bars (at mid-span of the intrados surface).

obtained results.

Since deflections of the CSA/GFRP segments are of the same order as deflection of OPC/Steel segment, the elastic energy accumulated in the CSA/GFRP segments are 1.4 and 1.8 times larger than OPC/Steel one, respectively, while the inelastic energy consumed prior to failure are 1.7 and 2.5 times smaller than the OPC/Steel reference.

The ductility index for the tested segments is reported in Table 5. CSA/GFRP segments exhibited a mean ductility index 54% lower than the OPC/Steel one, to be fundamentally ascribed to the reinforcement type (Steel/GFRP) rather than the concrete (OPC/CSA). Moreover, when considering the same GFRP reinforcement, a 42% rise in concrete strength resulted in a 29% reduction in ductility.

Based on the results, it is crucial to recognize that substantial deformations preceding failure do not necessarily imply ductility. The inelastic portion of the deformation, when present, is an essential component of ductility. Indeed, large deflections may result from the low elastic modulus of the GFRP and may correspond to a significant amount of elastic energy stored in the segment. Although the ductility index for the CSA/GFRP segments is lower than the one of the OPC/Steel segment, it is sufficient to guarantee the safety again the brittle failure. Indeed, in tunnels characterized by a large internal diameter, segments typically experience elevated bending moments during both transient phases and service stage. The latter typically constitutes the most challenging design condition. Conversely, the focus of this paper is on tunnels featuring a smaller internal diameter, which tend to be predominantly compressed during service. Such tunnels are less susceptible to asymmetric loads originating from soil or discontinuities. Consequently, the main reinforcement typically involves a minimum amount of rebars established by Codes to prevent brittle failure of the segments, especially during transient load situations, the latter are further introduced and extensively analyzed in the subsequent case study.

In accordance with CNR-DT203 [34], safeguarding against brittle failure is guaranteed by ensuring that the ultimate load (P_u) surpasses 1.5 times the cracking load (P_{cr}), as confirmed by the results reported in Table 5. This requirement can be expressed in terms of bending moments as the equivalent relation $M_u \geq 1.5 M_{cr}$, where M_u and M_{cr} denote the ultimate and cracking bending moments, respectively. Taking into account the concrete strength of the CSA/GFRP segment subjected to a bending test after 26 hours of aging, the recorded cracking bending moment is 65 kN•m. Notably, the ultimate bending moment, as reported in Table 5 and measuring 190 kN•m, surpasses the cracking bending moment by a factor of 2.9. This observation substantiates compliance with the provision of the Code, which incorporates a safety coefficient of 1.5.

To assess the effectiveness of the check procedure, Bending moment-Axial force interaction diagrams at the experimental ultimate state are derived in accordance with fundamental assumptions and constitutive
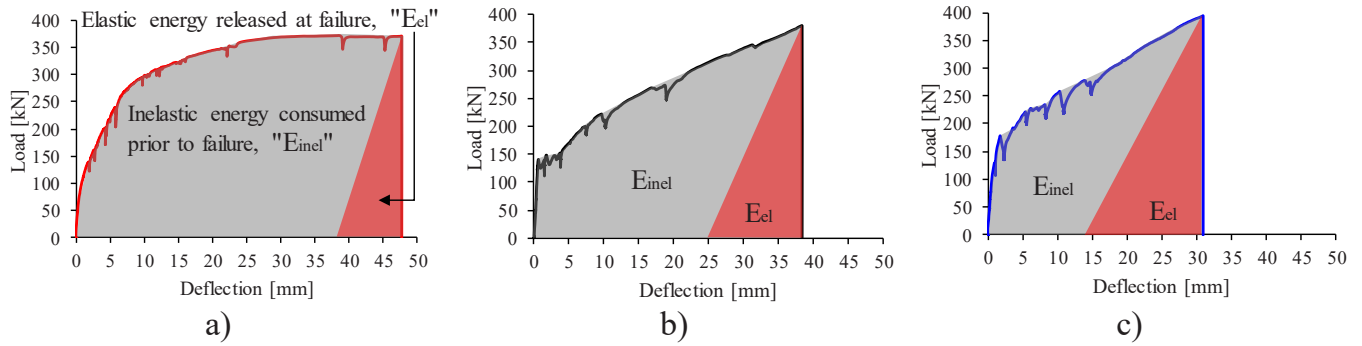
Fig. 11. Elastic and inelastic energy in the segments: a) OPC/Steel (28 days aged); b) CSA/GFRP (26 hours aged); and c) CSA/GFRP (15 days aged).

Table 5
Analytical and experimental results.

Segment solution	1st crack		Failure load			Failure moment			Deflection at failure	Ductility Index	Concrete strength
	$F_{1st,exp}$ [kN]	$w_{1st,exp}$ [mm]	$F_{max,ana}$ [kN]	$F_{max,exp}$ [kN]	ΔF [%]	$M_{u,ana}$ [kN•m]	$M_{u,exp}$ [kN•m]	ΔM [%]	δ [mm]	μ_e [-]	$f_{cm,cube}$ [MPa]
OPC/Steel	139	0.05	377	373	-1.0	188	186	-1.0	48	4.80	48
CSA/GFRP (I)	140	0.25	375	380	+1.3	187	190	+1.6	38	2.56	40
CSA/GFRP (II)	130	0.05	380	395	+3.9	190	197	+3.9	31	1.82	57

material stress-strain relationships as defined by EN 1992-1-1 [33] for concrete and steel, and CNR-DT 203/2006 [34] for GFRP. Specifically, the assumptions of planar section and perfect bond between GFRP/steel and concrete are imposed.

To replicate the actual experimental behaviour, mean values of material strength are adopted, and the strength-reduction coefficients are assumed to be equal to 1. The average material properties, utilized for the interaction diagrams, are summarized in Table 2 and Table 4. The bending moment-axial force interaction diagrams are depicted in Fig. 12a in which the design approach adopted for the CSA/GFRP segments, based on the same experimental performance in pure bending of the OPC/Steel reference one, is highlighted.

Regarding the detailed view of the bending moment-axial force interaction diagrams shown in Fig. 12b, the bending moments measured in the experimental tests are additionally superimposed [solid circle (•)]. As the solid circles (•) either lie on the related envelopes or deviate by less than six percent, as shown in Table 5 where the experimental strength values exceed the analytical ones, the simplified check procedure based on the bending moment-axial force interaction diagrams

appears suitable for predicting capacity.

Regarding the behavior of the segment under transient thrust exerted by TBM, full-scale point load tests were conducted at 30 hours and 28 days after segment casting for the CSA/GFRP (II) and OPC/Steel segments, respectively. The test was carried out according to one loading/unloading cycle with 250 kN increasing steps until the TBM service load equal to 1580 kN/pad.

The first crack occurred for splitting at load level of 500 kN and 750 kN (for each steel pad) with maximum crack width of 0.02 mm and 0.03 mm between green/red steel pads at the thrust side surface (red line in Fig. 13). As the load increased, the cracks moved on to the segments, as shown in Fig. 13. Arrived at the service load of 1580 kN/pad the maximum crack width was equal to 0.18 mm and 0.42 mm, respectively, as reported in Table 6 and Fig. 14b in which the evolution of the splitting cracks for the tested segments are superimposed.

At the conclusion of the test, when the thrust load was removed to simulate the end of segment installation by TBM, the maximum residual crack widths were measured at 0.10 mm and 0.15 mm for the OPC/Steel and CSA/GFRP segments, respectively as depicted in Fig. 14b. Although
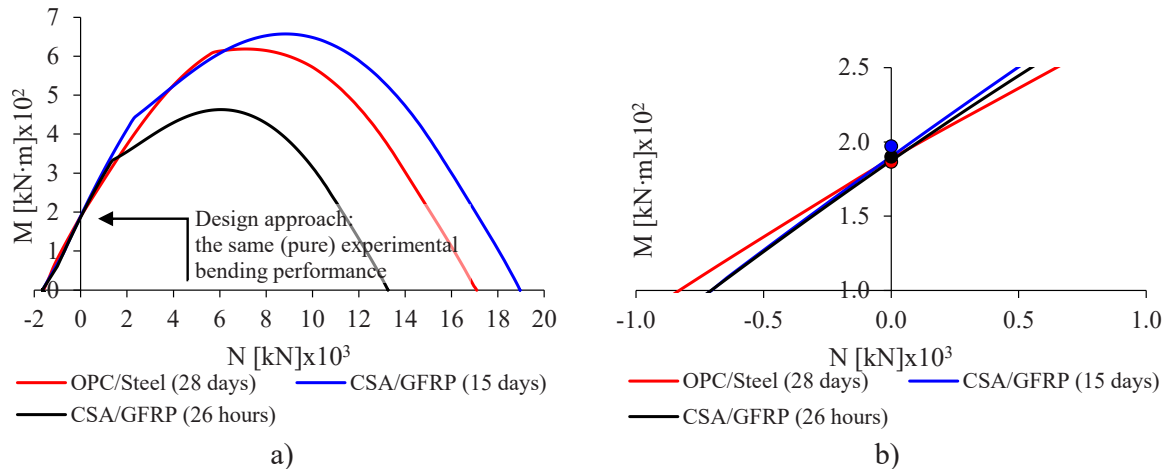

Fig. 12. Bending moment-Axial force interaction diagrams: a) Comparison of different solutions and design approach adopted for the CSA/GFRP segments; and b) Detail of the interaction diagrams with the superimposed bending moments measured experimentally.
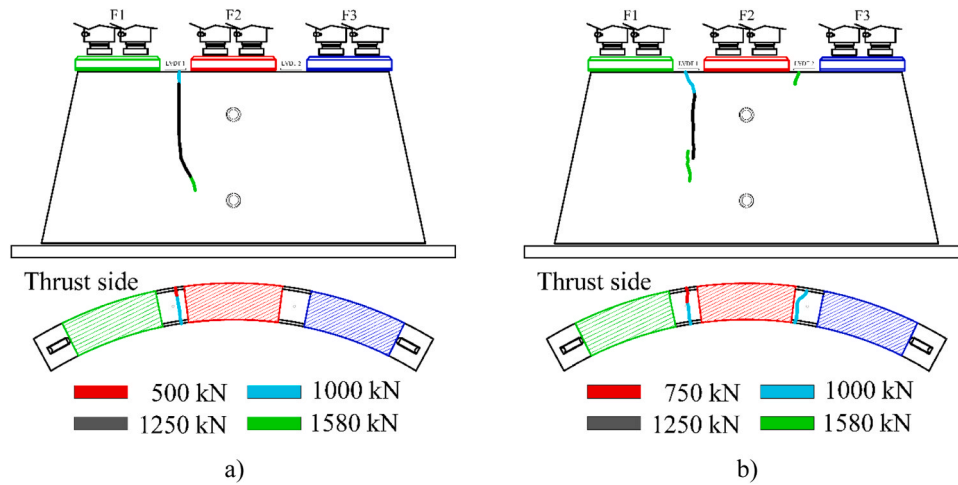
Fig. 13. Cracking patter at the TBM unloading: a) OPC/Steel reference segment (28 days aged); b) CSA/GFRP (II) segment (30 hours aged).

Table 6
Comparison of the crack width of the full-scale experimental results.

Segment solution	Load (500 kN)	Load (750 kN)	Service Load (1580 kN)	Unloading (0 kN)	Provision limit to unloading
	Maximum crack width [mm]			Residual crack width [mm]	
OPC/Steel	0.02	0.07	0.18	0.10	0.10
CSA/GFRP (II)	none	0.03	0.42	0.15	0.50

the crack width of the CSA/GFRP segment at the service load was 2.3 times greater than that of the OPC/Steel segment (still within the specified limit of 0.50 mm), it is worth noting that the elastic behavior of the reinforcement and its stiffness, comparable to that of the concrete, can facilitate the closure of the crack width at the end of the installation phase. This has been demonstrated by the authors in [38] and further confirmed by the residual crack widths reported in Table 6, where the widths reduced from 0.42 mm to 0.15 mm within five minutes of unloading. Analyzing the behavior of the reference segment, it can be observed that the high stiffness of the steel rebars, compared to that of the concrete (more than 6 times), does not offer the same advantages in terms of effectiveness in limiting residual crack widths, especially in aggressive environments where stricter provisions are typically required.

Furthermore, in order to conduct further experimental exploration in the future, it is advisable to incorporate supplementary GFRP reinforcement on the thrust side. This reinforcement will effectively counteract the splitting forces generated by the transient thrust forces exerted by TBM. This approach aligns with the current design criteria, which involves the use of supplementary steel reinforcement within that specific zone of the segment. By adopting this approach, it becomes feasible to substantially reduce the crack widths during the installation phases, as well as their residual values once the unloading is complete.

In Fig. 14a, the deformation behaviour of the segment with CSA-based concrete under the compression thrust exerted by the TBM is analyzed, comparing it to that of the reference segment composed of OPC-based concrete. The maximum compressive displacement at the service load for the CSA/GFRP segment was measured at 0.19 mm, slightly higher than the 0.18 mm observed for the OPC/Steel reference segment. However, in both cases, the segments showed the same trend in the loading/unloading cycle and fully recovered their deformation upon load removal. Based on the results obtained regarding cracking patterns and deformability, it can be confirmed that under transient TBM thrust the behaviour of the proposed CSA/GFRP system is comparable to that of the currently adopted OPC/Steel segment.

5. Case study

Throughout its service life, the tunnel lining commonly experiences prevalent compressive stresses. To prevent the occurrence of brittle failures during the temporary phases of tunnel lining construction,
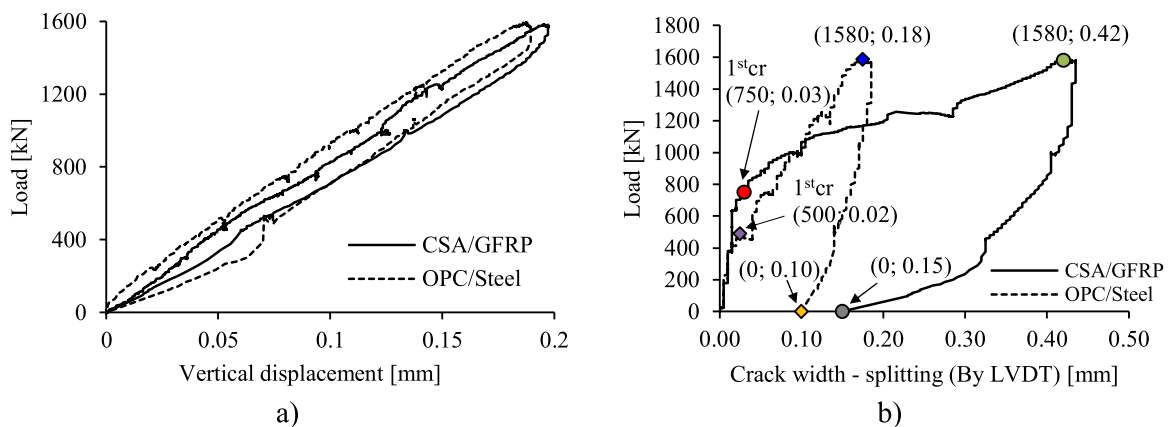

Fig. 14. Point load test results: a) Load versus average vertical displacement curves below each steel thrust pad; b) Crack-width evolution of the crack n.2 (between green and red steel thrust pads) during the loading/unloading steps.

reinforcement of the segments is crucial [39]. In this regard, a case study has been conducted to compare the design bending moments during the main construction phases with the structural capacity. The latter is defined by employing Bending moment-Axial force interaction diagrams. The Bending moment-Axial load interaction diagrams, as well as the bending moments associated with the various construction stages, have been established following the guidelines provided by Eurocode 2–1 [33] for concrete, fib Bulletin 83 [40], and ACI5447R-16 [41] for the respective analysis of these stages. Furthermore, the design of the GFRP reinforcement was based on CNR-DT 203–2006 [34]. It is worth mentioning that the complete metro tunnel ring consists of five segments together with one smaller key-segment.

In order to design the segmental lining, various load cases need to be taken into consideration. These include both temporary (transient phases) and permanent (final stage) conditions. The transient phases encompass demoulding, storage, and handling of the segments, while the final stage refers to the pressure exerted by the ground surrounding the tunnel lining. If the segments are manufactured directly on the construction-site, the transportation phase can be disregarded. Table 7 provides a summary of the acting forces (M_{Ed}, N_{Ed}, V_{Ed}) for each construction phase. It is important to note that the loads, material properties, and static schemes may vary across different phases.

In terms of material properties, the adoption of CSA/GFRP solution led to a specific requirement to expedite the phases from demoulding to segment installation. As a result, the characteristic (f_{ck}) and design (f_{cd}) compressive strength values (displayed in Table 7) remain the same for all transient phases. This differs from the information presented in fib Bulletin 83 [40], where the compressive strength for the common OPC/Steel segments is equal to the final design strength of the segments starting from the 28-day storage period until their installation. Regarding the final stage, the compressive strength values are lower compared to those typically used for this tunnel application that utilizes traditional concrete. This adjustment is driven by the need to accelerate the construction phases.

In the proposed case study, the final stage involves placing the longitudinal axis of the cross-sectional tunnel ring at a depth of 17.2 m below the countryside level. The net coverage of the tunnel ring is 14 m, as depicted in Fig. 14a. This stage also considers the presence of soil pressure and a building that directly interacts with the tunnel lining, which is a common condition encountered in metro tunnel construction projects. Additionally, it is assumed that there is no water table present.

The geotechnical analysis provides the necessary information about the axial forces (N_{Ed}) and bending moments (M_{Ed}) using the FLAC 8.0 software program [42]. The analysis is performed within the elastic-plastic field, utilizing a model based on the Mohr-Coulomb failure criterion with unassociated flow laws.

The load applied in the vertical direction corresponds to the geostatic load, while the load in the horizontal direction is determined based on the former, assuming an equal thrust coefficient at rest (K_0) of 0.426 ($K_0 = 1 - \sin(\varphi')$). The internal friction angle (φ') is taken as 35°, leading to the calculation of the horizontal load.

To account for the interference caused by the building, additional forces equivalent to 400 kN/m are applied to the foundation plane, which is positioned 4 m below the countryside level.

The stress and deformation state analysis took into consideration a long-term scenario. Static assessments were conducted under the simplified hypothesis that the excavation and lining of the tunnel are completed in a single calculation step. This approach aims to maximize the stresses on the tunnel lining. The findings of this analysis are consolidated in load case 4 of Table 7.

To ensure safety at the Ultimate Limit State (ULS), a Bending moment-Axial force interaction diagram is drawn for the segment. Fig. 15b presents the results, specifically focusing on the transient stages when the concrete is 5 hours old and the final stage when the segments have been installed for 2 days. In both cases, all the points representing the actions fall within the envelopes, indicating that the safety checks are met.

Additionally, the shear actions (V_{Ed}) are accounted for during each transient phase and are verified against the shear strength (V_{Rd}) as per the previous design Codes (Table 7, last two columns) for which the safety coefficient are 2.23, 1.01 and 5.09 for the transient cases and 2.01 for the final stage, respectively. Through this verification process, all the design checks are found to be satisfied.

6. CO₂ emissions of OPC/Steel and CSA/GFRP segments

Assessing the prospective impact of the tunnel adopting the proposed CSA/GFRP solution is imperative for promoting environmentally conscious design and steering the transition towards a more sustainable and eco-friendly economy. To achieve this goal, tools like Life Cycle Assessment (LCA) analysis can be employed to systematically and objectively identify design solutions with a lower environmental impact.

This study employs LCA to gauge the influence of diverse reinforcement (steel and GFRP) and concrete (OPC or A-CSA-OPC ternary system) configurations, as discussed in the preceding sections, on the climate change. The ensuing results pertain to the "Cradle to Gate" analysis configuration, named for its emphasis on tracing the life cycle from raw material extraction (Cradle) to the point at which the prefabricated segment departs from the manufacturing facility or it is manufactured directly on the construction-site (Gate), the latter depend to the solution accounted for. This analysis encompasses both the OPC/Steel solution, where the prefabricated segment is transported from the manufacturing facility, and the CSA/GFRP proposed solution, where the segment is directly realized on the construction-site. This approach encompasses an assessment of various intermediary production processes.

To guarantee the objectivity of the analysis, it is essential to establish

Table 7
Summary of required design checks and factors for transient and final stages (ULS) according to ACI544.7R-16.

Load Case	Phase	Dynamic shock factor	Key design parameter f_{ck} (f_{cd})	M_{Ed}	N_{Ed}	V_{Ed}	V_{Rd}
		β	(MPa)	(kN•m)	(kN)	(kN)	(kN)
1	Demoulding	2.0	15 (10)[b]	-17	0	48	107
2	Storage[a]	-	(5 hours)	-13	0	106	
3	Handling	2.0		-7	0	21	
4	Soil pressure (ULS)	-	30 (17)[c] (2 days)	56	711	67	135

Note:

(a) A possible temporary storage on construction-site (following demoulding) is taken into account;

(b) The design compressive strength (f_{cd}) at the transient stages is evaluate as $f_{cd} = \alpha_{cc}\dfrac{f_{ck}}{\gamma_c}$ by assuming the long-term coefficient α_{cc} equal to 1 and the safety coefficient of the concrete γ_c equal to 1.5;

(c) The design compressive strength (f_{cd}) at the final stage is evaluate as per the transient stages by assuming the long-term coefficient α_{cc} equal to 0.85;
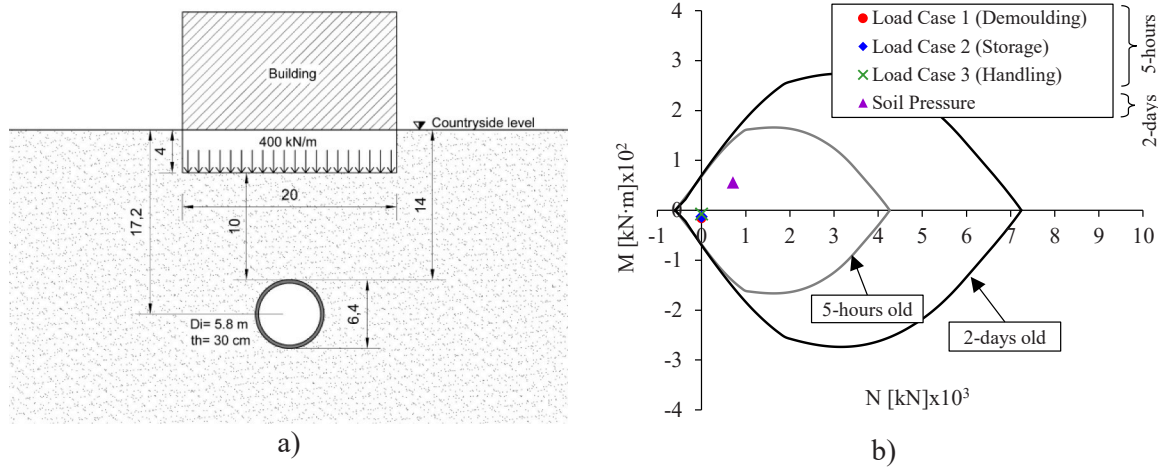
Fig. 15. a) Parameters adopted in FLAC analyses; and b) Safety check by means of Bending moment-Axial force interaction diagrams of transient and final stages.

a consistent methodology, ensuring the impartiality of the final results. In this context, international standardization is endorsed by UNI EN ISO 14040 [43], 14044 [44], and the Society of Environmental Toxicology and Chemistry (SETAC) [45]. These standards delineate distinct macro-phases: 1) Goal and scope definition; 2) Life Cycle Inventory – LCI; 3) Life Cycle Impact Assessment – LCIA; and 4) Life Cycle Interpretation.

The analyses pertaining to the study addressed in this paper were conducted using the SimaPro 9.2 software [46]. The computation was executed using the EN 15804+A2 method.

In this section, for the sake of brevity, macro-phases will not be presented in their entirety but will be outlined schematically for a better understanding of the issues related to the examined case from a sustainable design perspective. The "functional unit", defined as the reference for calculating the climate change, is the segment of the ring.

Concerning the goal and scope definition, the system boundaries are established in accordance with the construction supply chain outlined in UNI EN 15978 [47]. This delineation includes "product stage A," encompassing A1 (Raw material supply), A2 (Transport of raw materials), and A3 (Manufacturing of concrete/reinforcement and curing of the segment where applicable), as well as "Construction stage B," specifically A4 (Transportation from the manufacturing facilities to the precast plant/construction-site). It is crucial to note that the environmental impact of establishing the prefabrication plant on the construction-site for the CSA/GFRP solution is disregarded due to the complexity of its realization. In the future, this aspect should be considered for a more precise analysis.

Table 8 outlines the schematic inventory, encompassing the binder type for each examined solution (note: mix design constituents are the same for both solutions as reported in Table 1), the type of reinforcement and its incidence (I_R) relative to the selected functional unit, specifically the "segment".

A case study comparing the climate change in terms of CO_2 emissions of the conventional and new technology is presented in Fig. 16 and Table 9. The low-carbon CSA/GFRP solution emits 0.37 tCO_2/m^3 (approximately 0.50 tCO_2/segment) at the Product and Construction stages A1 to A4. Therefore, CO_2 emissions can be reduced by 35% compared to the conventional OPC/Steel solution for which the emissions are 0.57 tCO_2/m^3 (0.76 tCO_2/segment).

Based on the results, it can be observed that the improvement in terms of low carbon emissions does not stem from direct replacing OPC with the A-CSA-CEM II ternary system, which achieved a 2.7% reduction. Instead, the primary enhancement is attributed to substituting steel reinforcement with GFRP, leading to a 66% reduction in CO_2 emissions. From a sustainability standpoint, the greatest contribution in substituting OPC with the proposed ternary binder manifests through an indirect decrease in CO_2 emissions, attributed to the absence of steam-curing and reduced transportation (74% reduction in carbon emissions) required to convey the precast segments from the precast plant to the construction-site. This aspect contributes to enhanced sustainability in tunnel construction with the proposed CSA/GFRP solution, encompassing also a reduction in socio-economic impacts. Although not quantified in this study, socio-economic impacts, which are often overlooked, are deemed crucial for future evaluations and, along with the environmental impact, constitute the three primary pillars of sustainability. Lastly, it is noteworthy that the obtained delta in terms of CO_2 emission reduction between the traditional and proposed solutions, considering only the cementitious binder component, becomes even more pronounced if CEM I class cement, commonly used in the precasting of tunnel segments outside Italy, is adopted for the traditional

Table 8
Schematic inventory.

Segment Solution	Binder type	Reinforcement type	I_R			Steam-curing
			[kg/m^3]	[kg/segment[c]]	[%]	
OPC/Steel	CEM IV	Steel[a]	99	132	100	Yes
CSA/GFRP	A-CSA-CEM II	GFRP[b]	23	29	-78	No

Segment Solution	Transports
PC/Steel	Manufacturing facility → 565 km → Precast Plant → 47 km → Construction site
CSA/GFRP	Manufacturing facility → 248 km → Construction site

Note:

(a) Primary steel produced through an integrated process from iron ore. Raw data were obtained from the ecoinvent database of the SimaPro software based on European average data;

(b) GFRP bars consist of vinyl ester resin and E-CR glass fibers;
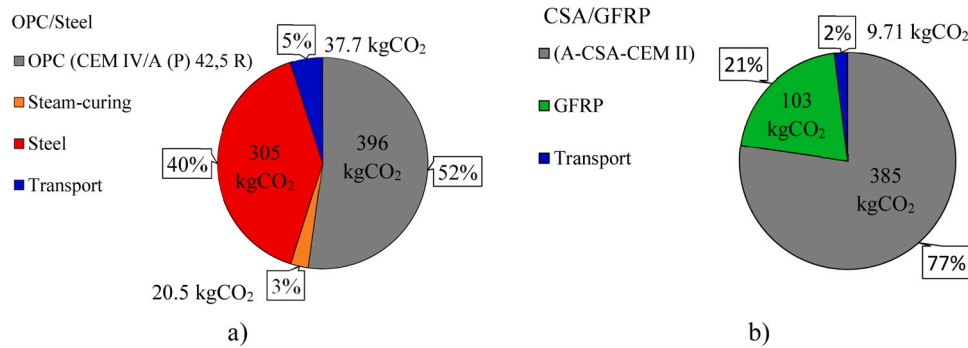
(c) Segment's volume = 1.33 m^3

Fig. 16. Comparison of CO_2 emission in product/construction stages (A1-A4): a) OPC/Steel segment; and b) CSA/GFRP segment.

Table 9
Climate change results for the production of a segment.

Segment Solution	Binder type	Reinf. type	Unit	Concrete	Reinf.	Steam-curing	Transport	Total	Δ [%]
OPC/Steel	CEM IV	Steel	kg CO_2eq	396	305	20.5	37.7	760	100
CSA/GFRP	A-CSA-CEM II	GFRP	kg CO_2eq	385	103	None	9.71	498	-35

solution.

7. Conclusions

This paper introduces a research study that investigates the structural performance of metro PCTL segments for which the conventional OPC-based concrete reinforced with steel bars has been replaced by CSA cement-based concrete combined with GFRP reinforcement.

Based on the experimental results, the theoretical study and the LCA analysis presented herein, the following conclusions can be drawn:

1. Based on the results derived from the conducted tests on the mix design, it is evident how CSA cements can significantly transform the prefabrication industry, establishing a more efficient and sustainable production cycle. Indeed, the substitution of OPC with the proposed ternary binder can offer significant operational benefits achieved through the elimination of steam-curing processes, enable faster mould shifting, leading to increased production per workshift and efficient clearing of storage areas, facilitating timely delivery for urgent orders, serving the TBM and its progress speed.
2. The increase in the compressive strength of concrete, although resulting in a reduction of ductility provided by the segment, has enhanced both the tensile effectiveness offered by GFRP bars in terms of the attained ultimate load and the efficiency in better controlling crack widths under flexural loading;
3. The utilization of elastic GFRP instead of elasto-plastic steel results in a ductility reduction of the segment, even though the ultimate deflections are comparable due to the lower elastic modulus of the non-metallic rebars with respect to the steel one. It is evident that, for safety considerations, it is essential to maintain a minimum level of ductility to prevent brittle failure. The primary challenge will lie in determining how to define this ductility specifically for segmented linings. To propose the GFRP as practical alternative to steel, it will be crucial to take into account the context in which these segments are designed and utilized. In the analysed case study, refers to a small-diameter tunnel, this diminished ductility is adequate to prevent brittle failures. Indeed, although transient phases represent the most severe conditions for the segments, they are typically exposed to statically determinate support configurations for which no stress redistribution is expected. This aspect can justify the possibility to rely a lower ductility index. Conversely, in the case of a large-diameter tunnel, the ductility could be increased by incorporating

fibers to concrete mix for a hybrid solution or neglected by increasing the ultimate design resistance with additional reinforcing GFRP bars.
4. The simplified check procedure based on the Bending moment-Axial force interaction diagrams is proven to be suitable for predicting the capacity of a tunnel segment using the CSA/GFRP system.
5. The deformation behaviour of the segment using CSA-based concrete under the compression thrust exerted by the TBM is similar to that of the reference segment made of OPC-based concrete. The maximum compressive displacement at the service load for the CSA/GFRP segment is comparable to that of the OPC/Steel reference segment. Both segments exhibit the same loading/unloading cycle trend and fully recover their deformation upon load removal. Based on the obtained results regarding cracking patterns and deformability, it can be confirmed that the behaviour of the proposed CSA/GFRP system is comparable to that of the currently used OPC/Steel segment under transient TBM thrust.
6. The analyzed case study has demonstrated that the CSA/GFRP system is capable of satisfying the design verifications related to the transient phases and the final stage experienced by the segment. This confirms the possibility of accelerating the construction phases of the tunnel, allowing for the production of in-situ segments and the installation of the tunnel lining as early as 2 days after casting, compared to the 28 days required for the traditional solution.
7. The CSA/GFRP technology developed in this study for the production of the PCTL segments seem to be one of the promising alternatives to the traditional solution until now used, showing a 35% reduction in carbon emissions and approaching the goal of the reduction value set for 2030 equal to −50% of emissions relating to the production and construction stages of a structure. Moreover, the adoption of non-metallic reinforcement will enable the elimination or significant reduction of tunnel maintenance and repair throughout it extended service life. This will result in a net-zero carbon emission balance for the structure. Thorough investigation of the "Use stage" in the Life Cycle Assessment (LCA) will be crucial, as it represents the main and delicate stage in the tunnel field. Indeed, unlike structures such as bridges and buildings, for tunnels, it is challenging to speak of an "end-of-life" that implies demolition and reconstruction of the tunnel, given the nature of the structural work. Therefore, for tunnels, the "use stage" could be considered perpetual, making the use of non-corrosive and less maintenance-intensive reinforcement much more effective and sustainable in the long-term perspectives. In case of demolitions needed to modify the tunnel geometry for the construction of new metro stations or the realization of safety niches,

bypasses, escape routes, or ventilation channels, the demolitions of the CSA/GFRP-based tunnel lining are facilitated by the fact that special and expensive cutting machines are not required, given the low shear strength offered by GFRP reinforcement. This significantly reduces demolition times, and compared to traditional solutions, the demolished tunnel portions offer easier disposal, as concrete and GFRP reinforcement can be disposed or recycled together without the need for separation, as is the case for steel-reinforced lining.

8. The possibility of in-situ pultrusion of GFRP bars, the rapid curing provided by CSA cement-based concrete, and reduced stacking space allow on-site full prefabrication. This approach enhances both environmental than socio-economic impacts by reducing pollution and traffic congestion in urban areas due to the transports of reinforcement cages and segments from manufacturing plants to prefabrication sites and construction sites.

9. Finally, the use of ternary binders based on CSA may enable a reduction in the amount of binder needed to attain the same strength class as equivalent Portland-based concrete, typically adopted for the PCTL segments. This, in turn, facilitates a further decrease in the climate change of CSA-based mixes and could present a potential solution to address the challenges faced by the cement industry in the near future. Additional research should be conducted to assess the performance of the mix design with a reduced amount of ternary binder based on CSA.

Funding

CRediT authorship contribution statement

Simone Spagnuolo: Writing – original draft, Validation, Software, Project administration, Methodology, Investigation, Formal analysis, Data curation, Conceptualization. **Alberto Meda:** Writing – review & editing, Resources, Supervision, Funding acquisition.

Declaration of Competing Interest

The authors declare that they have no known competing financial interests or personal relationships that could have appeared to influence the work reported in this paper.

Data availability

Data will be made available on request.

Acknowledgments

References

[1] Tunnel Market Survey 2019. ITA-AITES. c/o MIE (Maison Internationale de l'Environnement). Chemin de Balexert 9 - CH-1219 Châtelaine – Switzerland.

[2] R. Kajaste, M. Hurme, Cement industry greenhouse gas emissions - management options and abatement cost, J. Clean. Prod. 112 (2016) 4041–4052, https://doi.org/10.1016/j.jclepro.2015.07.055.

[3] B.J. van Ruijven, D.P. van Vuuren, W. Boskaljon, M.L. Neelis, D. Saygin, M.K. Patel, Long-term model-based projections of energy use and CO2 emissions from the global steel and cement industries, Resour. Conserv. Recycl. 112 (2016) 15–36, https://doi.org/10.1016/j.resconrec.2016.04.016.

[4] J.L. Galvez-Martos, R. Chaliulina, A. Elhoweris, J. Mwanda, A. Hakki, Y. Al-horr, Techno-economic assessment of calcium sulfoaluminate clinker production using elemental sulfur as raw material, J. Clean. Prod. 301 (2021) 2021, https://doi.org/10.1016/j.jclepro.2021.126888.

[5] WBCSD and IEA Cement Technology Roadmap 2009: Carbon Emissions Reductions up to 2050. ISBN: 978-3-940388-47-6.

[6] K.L. Scrivener, V.M. John, E.M. Gartner, Eco-efficient cements: potential economically viable solutions for a low-CO2 cement-based materials industry, Cem. Concr. Res. 114 (2018) 2–26, https://doi.org/10.1016/j.cemconres.2018.03.015.

[7] M.A.G. Aranda, A.G. De la Torre, 18. Sulfoaluminate cement, in: F. Pacheco-Torgal, S. Jalali, J. Labrincha, V.M. John (Eds.), Eco-Efficient Concrete, Woodhead Publishing, 2013, pp. 488–522, https://doi.org/10.1533/9780857098993.4.488.

[8] Q. Yuan, K. Liu, K. Zheng, C. Ma, Chapter 2 - Inorganic cementing materials, Civ. Eng. Mater. (2021) 17–57, https://doi.org/10.1016/B978-0-12-822865-4.00002-7.

[9] Y. Tao, A.V. Rahul, M.K. Mohan, G. De Schutter, K.V. Tittelboom, Recent progress and technical challenges in using calcium sulpoaluminate (CSA) cement, Cem. Concr. Compos. 137 (2023) 2023, https://doi.org/10.1016/j.cemconcomp.2022.104908.

[10] J. Pooni, D. Robert, F. Giustozzi, S. Setunge, Y.M. Xie, J. Xia, Novel use of calcium sulfoaluminate (CSA) cement for treating problematic soils, Constr. Build. Mater. 260 (2020) 120433, https://doi.org/10.1016/jconbuildmat.2020.120433.

[11] A. Więckowski, 2020. Automating CSA cement-based reinforced monolithic ceiling construction. Autom. Construct. 111 (2020), 103051, ⟨https://doi.org/10.1016/j⟩. autcon.2019.103051.

[12] F. Bertola, D. Gastaldi, S. Irico, G. Paul, F. Canonico, Influence of the amount of calcium sulfate on physical/mineralogical properties and carbonatation ressitance of CSA-based cements. Cem. Concr. Res. 151 (2022) 2022, https://doi.org/10.1016/j.cemconres.2021.106634.

[13] S. Ioannou, K. Paine, L. Reig, K. Quillin, Performance characteristics of concrete based on ternary calcium sulfoaluminate-anhydrite-fly ash cement, Cem. Concr. Comp. 55 (2015) 196–204, https://doi.org/10.1016/j.cemconcomp.2014.08.009.

[14] L. Zhang, F.P. Glasser, Investigation of the microstructure and carbonation of CSA-based concretes removed from service, Cem. Concr. Res. 35 (12) (2005) 2252–2260, https://doi.org/10.1016/j.cemconres.2004.08.007.

[15] P. Duan, W. Chen, J. Ma, Z. Shui, Influence of layered double hydroxides on microstructure and carbonation resistance of sulphoaluminate cement concrete, Constr. Build. Mater. 48 (2013) 601–609, https://doi.org/10.1016/j.conbuildmat.2013.07.049.

[16] H. Geng, P. Duan, W. Chen, Z. Shui, Carbonation of sulphoaluminate cement with layered double hydroxides, J. Wuhan. Univ. Technol. - Mater. Sci. Ed. 29 (2014) 97–101, https://doi.org/10.1007/s11595-014-0874-y.

[17] V. Afroughsabet, L. Biolzi, P.J.M. Monteiro, M.M. Gastaldi, Investigation of mechanical and durability properties of sustainable high-performance concrete based on calcium sulfoaluminate cement, J. Build. Eng. Vol. 43 (2021) 102656, https://doi.org/10.1016/j.jobe.2021.102656.

[18] B. Benmokrane, P. Wang, T.M. Ton-That, H. Rahman, J.F. Robert, Durability of glass fiber-reinforced polymer reinforcing bars in concrete environment, J. Compos. Constr. 6 (3) (2002) 143–153, https://doi.org/10.1061/(ASCE)1090-0268(2002)6:3(143).

[19] Y. Chen, J.F. Davalos, H.-Y. Kim, Accelerated aging tests for evaluations of durability performance of FRP reinforcing bars for concrete structures, Compos. Struct. 78 (1) (2007) 101–111, https://doi.org/10.1016/j.compstruct.2005.08.015.

[20] O. Gooranorimi, A. Nanni, GFRP reinforcement in concrete after 15 years of service, J. Compos. Constr. Vol. 21 (5) (2017), https://doi.org/10.1061/(ASCE)CC.1943-5614.0000806.

[21] S. Ramanathan, V. Benzecry, P. Suraneni, A. Nanni, Condition assessment of concrete and glass fiber reinforced polymer (GFRP) rebar after 18 years of service life, Case Stud. Constr. Mater. 14 (2021) (2021) e00494, https://doi.org/10.1016/j.cscm.2021.e00494.

[22] A.R. Emparanza, R. Kampmann, F. De Caso, C. Morales, A. Nanni, Durability assessment of GFRP rebars in marine environments, Constr. Build. Mater. 329 (2022) 2022, https://doi.org/10.1016/j.conbuildmat.2022.127028.

[23] P. Wang, H.-L. Wu, L.-Y.-W. Ke, C.K.Y. Leung, Mechanical and long-term durability prediction of GFRP rebars with the adoption of low-pH CSA concrete, Constr. Build. Mater. 346 (2022) 2022, https://doi.org/10.1016/j.conbuildmat.2022.128444.

[24] A. Caratelli, A. Meda, Z. Rinaldi, S. Spagnuolo, G. Maddaluno, Optimization of GFRP reinforcement in precast segments for metro tunnel lining, Compos. Struct. 181 (2017) 336–346, https://doi.org/10.1016/j.compstruct.2017.08.083.

[25] S. Spagnuolo, A. Meda, Z. Rinaldi, A. Nanni, Precast concrete tunnel segments with GFRP reinforcement. ASCE, J. Compos. Constr. 21 (5) (2017) 2017, https://doi.org/10.1061/(ASCE)CC.1943-5614.0000803.

[26] S. Spagnuolo, A. Meda, Z. Rinaldi, A. Nanni, Curvilinear GFRP bars for tunnel segments applications, Compos. Part B: Eng. 141 (2018) 137–147, https://doi.org/10.1016/j.compositesb.2017.12.038.

[27] S.M. Hosseini, S. Mousa, H.M. Mohamed, B. Benmokrane, Structural Behavior of Precast RC Tunnel Segments with GFRP Bars and Ties Under Bending Load, Acids Struct. J. 119 (1) (2022) 1–13. ⟨https://doi.org/10.14359/51734143⟩.

[28] B. Ibrahim, S. Mousa, H.M. Mohamed, B. Benmokrane, Quasi-static cyclic behaviour of precast high-strength concrete tunnel segments reinforced with GFRP bars. Eng. Struct. 286 (2023) 2023, https://doi.org/10.1016/j.engstruct.2023.116159.

[29] Standard U.N.I. EN 15978:2011. Sustainability of construction works - Assessment of environmental performance of buildings - Calculation method.

[30] A. Kasuga, Impact of carbon neutrality on structural concrete – not a risk but an opportunity, Struct. Concr. 24 (2) (2022) 1725–1736, https://doi.org/10.1002/suco.202200838.

[31] Standard U.N.I. 11307:2008. Testing for hardened concrete – Shrinkage determination.

[32] A.E. Naaman and S.M. Jeong, Structural ductility of concrete beams prestressed with FRP tendons, in: Proc. 2nd Int. RILEM Symp. On Non-Metallic (FRP) Reinforcement for Concrete Structures, RILEM, France, 1995, pp. 379-386.

[33] EN 1992-1-1:2004 Eurocode 2: Design of concrete structures - Part 1-1: General rules and rules for buildings.

[34] CNR (Italian National Research Council). (2007). Guide for the Design and Construction of Concrete Structures Reinforced with Fiber-Reinforced Polymer Bars. CNR DT 203-2006, Rome, Italy.

[35] American Concrete Institute (ACI) (2015). Guide for Design and Construction of Structural Concrete Reinforced with Fiber-Reinfroced Polymer (FRP) Bars. ACI 440.1R-15, Farmington Hills, MI.

[36] Canadian Standars Association (CSA). (2012). Design and Construction of building components with fiber-reinforced polymers. CAN/CSA-S806-S812, Mississauga, ON, Canada.

[37] Canadian Standars Association (CSA). (2019). Canadian Highway Bridge Design Code. CAN/CSA-S6-S19, Mississauga, ON, Canada.

[38] A. Meda, Z. Rinaldi, S. Spagnuolo, C.M. Eddie, Behaviour of FRC segments with GFRP cage under TBM thrust in presence of GAPs, Tunn. Undergr. Space Technol. 107 (2021) (2021) 103669, https://doi.org/10.1016/j.tust.2020.103669.

[39] V. Cugat, S.H.P. Cavalaro, J.M. Bairán, A. de la Fuente, Safety format for the flexural design of tunnel fibre reinforced concrete precast segmental linings, Tunn. Undergr. Space Technol. 103 (2020) (2020) 103500, https://doi.org/10.1016/j.tust.2020.103500.

[40] fib (Fédération Internationale du Béton). (2017). Precast Tunnel Segments in Fibre-Reinforced Concrete. *Fib* Bulletin 83, Lausanne, Switzerland.

[41] ACI (American Concrete Institute). (2016). Report on Design and Construction of Fiber-Reinforced Precast Concrete Tunnel Segments. ACI 544.7R-16, Farmington Hills, MI.

[42] ICG (Itasca Consulting Group). (2015). FLAC (Fast Lagrangian Analysis of Continua) version 8.0. Minneapolis.

[43] UNI EN ISO 14040:2021. Environmental management – Life cycle assessment – Principles and framework (2022).

[44] UNI EN ISO 14044:2021. Environmental management – Life cycle assessment – Requirements and guidelines (2023).

[45] SETAC, «Society of Environmental Toxicology and Chemistry» [Online]. Available on: ⟨https://www.setac.org/⟩.

[46] Product Ecology Consultants, "SimaPro" Product Ecology Consultants. (2023).

[47] UNI EN 15978:2011. Sustainability of construction works – Assessment of environmental performance of buildings - Calculation method (2011).

[48] UNI EN 12350-6:2019. Testing fresh concrete – Part 6: Density.

[49] UNI EN 12350-2:2019. Testing fresh concrete – Part 2: Slump test.

[50] UNI EN 12390-3:2019. Testing hardened concrete – Part 3: Compressive strength of test specimens.

[51] ASTM D7205/D7205M-21. Standard Test Method for Tensile Properties of Fiber-Reinforced Polymer Matrix Composite Bars. ASTM International, (2021).